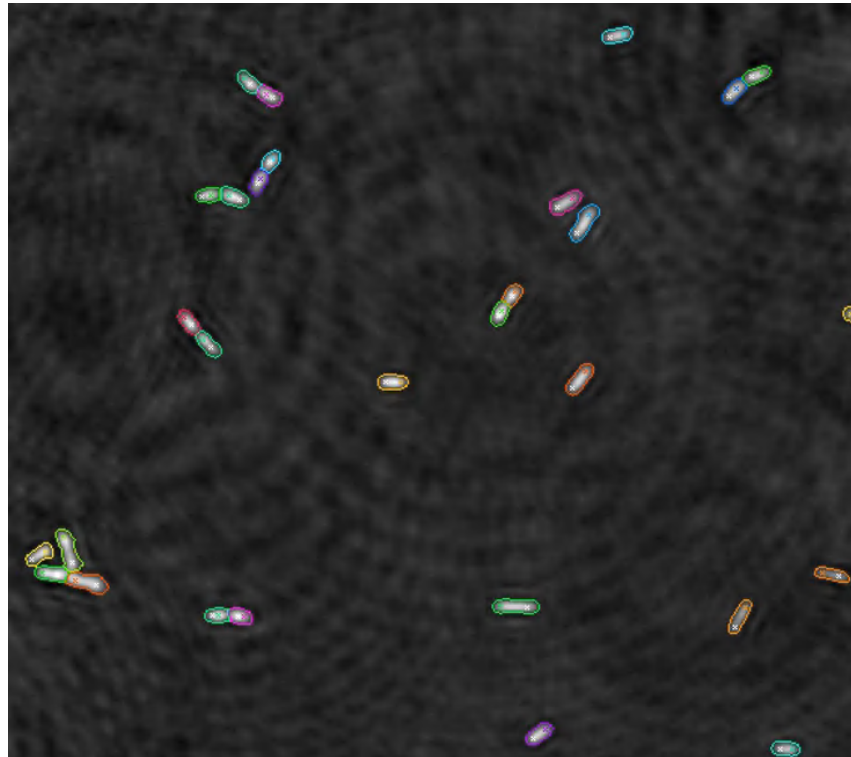


MASTER THESIS

Fabian Braun

MSc Mechanical Engineering

IMAGING PIPELINE FOR DHM



27 February - 11 September 2023

Prof. Dr. Roman Stocker

Advised by:

Dr Richard Henshaw

Dieter Baumgartner

Environmental Microfluidics Group

Institute of Environmental Engineering, ETH Zürich

ETH Zürich



Acknowledgements

I am deeply thankful for the invaluable learning experience this master's thesis has provided me. It allowed me to enhance my coding skills, deepen my comprehension of light-related concepts, and make meaningful contributions to an exciting project. First and foremost I want to thank Dieter Baumgartner for supervising me and thereby allowing me to do this project. Secondly I want to thank Richard Henshaw's for his useful insights and support. Both Dieter Baumgartner's and Richard Henshaw's are knowledgeable, easy going and funny which made every interaction with them truly enjoyable. Lastly, I extend my gratitude to Prof. Dr. Roman Stocker for granting me the opportunity to undertake this master's thesis within the Environmental Microfluidics Group.

September 2023
Fabian Braun

Contents

Abstract	1
1 Introduction	2
2 State of the art	3
2.1 Quantitative phase imaging	3
2.1.1 Historical foundations of phase imaging	3
2.1.2 Types of QPI	4
2.1.3 Digital holographic microscopy	5
2.1.4 Focus distance	7
2.1.5 Limitations	7
2.1.6 Phase shift to cellular dry mass conversion	8
2.2 Segmentation and tracking	8
2.2.1 Interactive learning and segmentation toolkit	8
2.2.2 Deep Learning for Time-lapse Analysis	9
2.2.3 U-Net	9
3 Material and methods	11
3.1 From hologram to a clean phase image	11
3.1.1 Construction of the phase image	11
3.1.2 Surface plane subtraction	11
3.1.3 Focusing	13
3.1.4 Background subtraction and spatial averaging	15
3.2 Bacteria segmentation and lineage tracking	16
3.2.1 Preparing training data with llastik	16
3.2.2 DeLTA: segmentation and tracking	18
4 Results	20
4.1 Phase image construction	20
4.1.1 Surface plane Subtraction	20
4.1.2 Focusing	21
4.1.3 Background Subtraction	21
4.1.4 Spatial averaging	22
4.1.5 Overall Improvements: pixel errors	23
4.1.6 Focusing effect on bacteria's mass	23

4.2 Segmentation and tracking with DeLTA	24
4.3 Cell cycles	27
5 Discussion	29
5.1 Phase image	29
5.2 Segmentation and lineage tracking	29
6 Conclusion and outlook	30

List of Figures

1	DHM setup	6
2	U-Net architecture	10
3	surface plane fitting	12
4	Reconstruction focus	14
5	Spatial averaging line	15
6	Ilastik pixel classification	16
7	Ilastik object detection	17
8	DeLTA pixel weights	19
9	Surface plane subtraction results	20
10	Focusing results	21
11	Background subtraction results	22
12	Spatial averaging results	22
13	Pixel error results	23
14	Mass decrease from out-of-focus images	24
15	Hyperparameter tuning	25
16	Training history	26
17	Segmentation errors	26
18	Implausible cell cycles	27
19	Valid cell cycles	28

List of Abbreviations

CCD	charge coupled device
DeLTA	Deep Learning for Time-lapse Analysis
DHM	digital holography microscopy
Ilastik	interactive learning and segmentation toolkit
QPI	Quantitative phase imaging

Abstract

In this thesis an image processing pipeline tailored to time-lapse images of bacterial growth using digital holographic microscopy (DHM) is presented. The pipeline interacts with the software Koala to reconstruct phase images from holograms, making the storage of individual phase and intensity images unnecessary. A new focusing method for the bacterial plane is introduced. It then uses spatial averaging to improve the noise level.

Segmentation and tracking of the bacteria lineage is done with the help of U-Nets, a relatively new type of deep neural network (2015), that is the current standard in biological image processing. DeLTA, an image processing pipeline based on U-Nets, is used, making interaction and the output files easy to use. The training data for the U-Nets is semi automatically produced with Ilastik. Even under suboptimal experimental conditions, the resultant segmentation and tracking demonstrate robust performance for individual bacteria. But challenges arise when multiple bacteria coalesce, leading to instances of unrecognized bacteria or to merging of separate bacteria.

The pipeline seamlessly integrates reconstruction, segmentation, and tracking without requiring manual intervention, yet affording the flexibility for knowledgeable operators to make various parameter adjustments as needed.

1 Introduction

Biology has made significant advancements in recent years, largely thanks to better computers. With new technology, data can be collected faster than ever before. This makes it crucial to find efficient ways to analyze all this data. In this work, an image pipeline is introduced that helps to track how bacteria grow, starting with pictures taken using digital holographic microscopy (DHM). The pipeline consists of several individual processes that were already in use before the start of this work. Some were included without change, while others have been improved to enhance their effectiveness.

Biomass estimation often entails measuring bacteria's length and calculating their volume. Biomass is then estimated from the volume by assuming a constant dry mass density factor (Taheri-Araghi et al., 2017; Zheng et al., 2020). However, this method is inherently imprecise as bacteria may exhibit varying widths for the same length. Additionally, it has been established that bacterial density is not a constant parameter (Oldewurtel et al., 2021a).

In contrast, the phase images generated through DHM offer a more accurate quantitative measurement method for bacterial mass. This approach uses the principle that the speed of light within a material is inversely proportional to its density. Light passing through a bacteria will travel slower than light in the surrounding medium, resulting in an optical path difference. By integrating this optical path difference over the bacteria's area and applying a constant factor, an accurate estimate of the bacterial mass can be derived.

A time-lapse series of phase images is employed to track the dynamic growth processes of bacteria. This pipeline uses a U-Net, a neural network architecture that has become the standard for biological image processing. Specifically, the DeLTA (Deep Learning for Time-lapse Analysis) image pipeline, initially designed for phase contrast images, has been adapted for phase difference images to provide a robust framework for bacterial growth analysis.

2 State of the art

2.1 Quantitative phase imaging

Quantitative phase imaging (QPI) is an imaging method that allows measurements of the optical thickness in transparent or semi-transparent specimens, providing valuable insights into biological samples. It gained prominence in the study of cells and tissues. Unlike traditional fluorescence microscopy, QPI does not require labeling, resulting in reduced phototoxicity and no photobleaching. The images produced by QPI offer quantitative data, providing an objective view of morphology and dynamics without the influence of contrast agents. Over the past decade, advancements in QPI technology have led to its adoption in biomedical labs, shifting the focus from technology development to practical applications.

2.1.1 Historical foundations of phase imaging

In 1873, Abbe introduced the first theory of image formation in optical microscopy, proposing that images are formed by the superposition of waves from different angles, resulting in an interferogram (Park et al., 2018). This theory suggested that microscopes couldn't resolve objects smaller than half the wavelength of propagating waves (Rosenthal et al., 2009). Contrast, a crucial aspect of imaging, determines how distinct an object appears against its background. For biological specimens, the contrast is primarily influenced by light scattering, which depends on the specimen's thickness and refractive index variations. In the visible spectrum, most biological cells and tissues don't absorb much light. If a specimen scatters too little light, its structure becomes hard to discern against the incident light. Conversely, excessive scattering can obscure the image. Specimens like single cells, which scatter light weakly, are termed 'phase objects' because they mainly affect the light's phase, not its amplitude. To visualize these, they were often converted into 'amplitude objects' using stains or fluorescent tags. (Park et al., 2018).

In the 1930s Zernike found that adding an additional phase shift to the scattered field increases the contrast of phase objects. This can be shown by decoupling the incident and the scattered fields. The total field U without phase shift is given by:

$$U(x, y) = |U|e^{i\phi(x, y)} \approx |U| [1 + i\phi(x, y)] \quad (1)$$

where $\phi(x, y)$ is the phase delay. It can be seen that the intensity of such an object, $|U|^2$, shows little spatial modulation, which means, little contrast. Whereas the total field with phase shift is:

$$U_{PC}(x, y) = |U| \{1 + i[i\phi(x, y)]\} \approx |U|e^{-\phi(x, y)} \quad (2)$$

where U_{PC} is the phase contrast image. It can be seen that the phase difference has a much bigger effect on the image intensity $|U|^2$ with the phase shift (Park et al., 2018). This effect is used in phase contrast microscopy.

In 1948 Gabor found that the recording of the intensity of the light emerging from an object at an out-of-focus plane incorporates both the amplitude and phase information. It was called holography, a combination of the Greek words "holos" meaning whole and "gramma" meaning message, since it captures the complete information of the light. In his setup he illuminated an object with coherent light. The light that reflects off the illuminated object then combines with a reference beam of coherent light. This combination of light waves creates an interference pattern, which carries information about the object's shape and structure. Gabor recorded this interference pattern on a photosensitive film. After exposure, a chemical development process fixes the interference pattern on the film, preserving the encoded phase and amplitude information. To view the hologram, one can illuminate the developed holographic plate with the same coherent light used during recording. When this light interacts with the developed hologram, it recreates the original interference pattern. The object appears in focus at the same distance as when it was recorded (Gábor, 1948). This method has severe limitations, because in addition to the in-focus image, the method always generates an overlapping out-of-focus twin image. These images can later not be separated (Park et al., 2018). This twin image limitation was later solved by using an off-axis incident field, meaning that the object beam and the reference beam are at an angle (Leith and Upatnieks, 1962). This shifts the unwanted twin image onto a different axis with respect to the in-focus image (Park et al., 2018).

2.1.2 Types of QPI

The methods in quantitative phase imaging differ in several characteristic, each with advantages and disadvantages.

One distinction is whether the reconstructed image is tomographic. In tomographic methods several images from different angles around the samples are taken. During the imaging process either the object or the light equipment is rotated around (Cacace et al., 2020). Using these images, a "true" three-dimensional object can be computed. In some experiments, like cell studies, the three-dimensional image is worth the increase in complexity (Yang et al., 2017; Kim et al., 2014; Kuš et al., 2014).

Non-tomographic images are composed by a single image from only one side. They can be constructed via point scanning techniques or as a full-field image. In point scanning techniques individual points are lighted in succession. Point-scanning techniques benefit from the ease of implementation but suffer from low throughput and noise introduced by the mechanical instability of the scanning process (Park et al., 2018).

Another big distinction is whether the QPI technique is interferometric or not. In interferometric techniques, a reference beam is added to the object beam to create an interference pattern. This pattern is then used to evaluate the original phase map. A main advantage of the non-interferometric techniques is that the setup is easier, since there is no reference beam needed. However, the mathematical reconstruction of the wavefront can also get stuck in local minima (Fienup, 1982).

Interferometric QPIs can further be categorised into holographic and non-holographic. In non-holographic methods the interferograms are obtained directly in the focal plane. The phase image is then calculated for this plane only. In holographic images the interferograms are obtained in an out-of-focus plane. There, a wavefront is calculated, which then can be propagated back into the focus.

The last characteristic is whether the refractive beam and the object beam are parallel when hitting the camera, called in-line, or at an angle, called off-axis. Both of them use different methods to get rid of the 'twin-image'. The in-line method uses temporal modulations, whereas off-axis uses spatial modulations (Park et al., 2018). In-line methods use several images with different phase shifts between the object and the reference wave to construct the hologram or phase image. This decreases the throughput significantly (Park et al., 2018). Another challenge of this method is the precise shifting of the beam. An advantage is that there are closed-form solutions for the phase image (Cacace et al., 2020). An example of this is spatial light interference microscopy (SLIM). SLIM is a 2D, full-field, interferometric, non-holographic, in-line method. For this method the images with phase shifts corresponding to $\omega\tau = 0, \frac{\pi}{2}, \pi, \frac{3\pi}{2}$ are needed.

$$\Delta\phi(x, y) = \tan^{-1} \left[\frac{I_{\frac{3\pi}{2}}(x, y) - I_{\frac{\pi}{2}}(x, y)}{I_0(x, y) - I_\pi(x, y)} \right] \quad (3)$$

where $\Delta\phi(x, y)$ is the phase difference map and I_x are the intensity images at the various phase shifts. Further calculating the phase map with:

$$\phi(x, y) = \tan^{-1} \left[\frac{\beta(x, y)\sin(\Delta\phi(x, y))}{1 + \beta(x, y)\cos(\Delta\phi(x, y))} \right] \quad (4)$$

where $\beta(x, y) = |U_1(x, y)|/|U_0|$ and U_1, U_0 are the scattered and unscattered fields (Wang et al., 2011).

In contrast, off-axis interferometry, used also in DHM, utilizes spatial modulations. An off-axis angle introduces a distinct spatial frequency. The desired phase map is encapsulated within a cross-term, with the spatial frequency serving as its modulation frequency. Using a Fourier transformation, this cross-term can be singled out, enabling computation of the phase map. This method requires just a single image, which facilitates high-speed imaging. A downside of this method is that it comes at a spatial cost, since the phase image is only calculated on a single sideband of Fourier transformed images (Park et al., 2018).

2.1.3 Digital holographic microscopy

The DHM configuration utilized in this thesis is a modified version of the DHM initially introduced by Cuche et al. in 1999. DHM is a 2D, full-field, interferometric, holographic method. While it can also be in-line, the version used in this thesis is off-axis. In the original DHM the object beam reflects off a non-transparent object, the variation adopted in our experiments accommodates transparent objects (Cuche et al., 1999a).

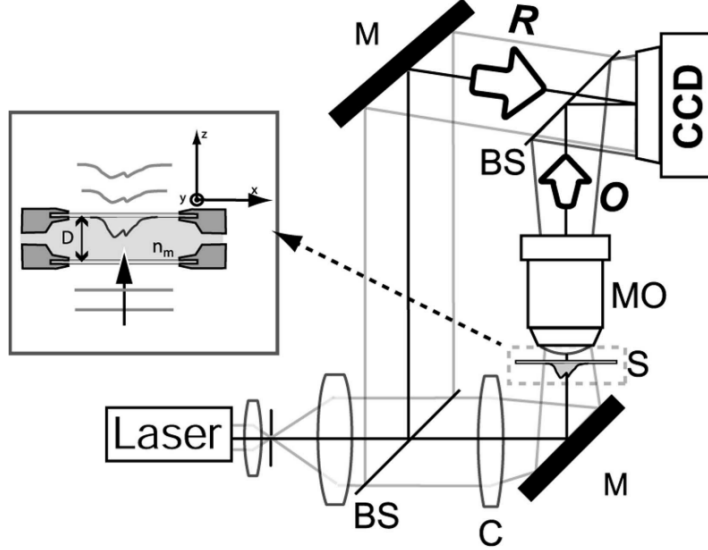


Figure 1: This is the simplified representation of a DHM setup. A laser beam is split into a reference beam and an objective beam. The reference beam is guided directly into a CCD camera, whereas the objective beam first passes the sample and a Microscope. Both beams form an interference pattern on the camera called hologram.

The DHM, shown in Figure 1, essentially operates like a Mach–Zehnder interferometer. A laser beam, after being expanded, is directed through a beam splitter, which divides it into the reference and object beams. The reference beam is guided into the CCD camera with the help of a mirror. The object beam first travels through a condenser and subsequently through the sample, after which it is gathered by the microscope objective. Both the reference wave, $\mathbf{R}(x, y)$ and the object wave, $\mathbf{O}(x, y)$, are eventually combined at an angle onto a CCD camera, resulting in an interference pattern called hologram (Marquet et al., 2005). The light intensity of the hologram is described by the equation:

$$I_H(x, y) = |\mathbf{R}|^2 + |\mathbf{O}|^2 + \mathbf{R}^* \mathbf{O} + \mathbf{R} \mathbf{O}^* \quad (5)$$

where * is the complex conjugate.

In classical holography reconstruction is achieved by illumination of the hologram with a replica of the reference wave. A wavefront $\psi = \mathbf{R}(x, y)I_H(x, y)$ is transmitted by the hologram and propagates toward an observation plane, where a three-dimensional image of the object can be observed (Cuche et al., 1999a). Here the reconstruction is done digitally with a computed reference wave $\mathbf{R}_D(k, l)$ resulting in:

$$\Psi(k\Delta x, l\Delta y) = \mathbf{R}_D(k, l)I_H(k, l) = \mathbf{R}_D|\mathbf{R}|^2 + \mathbf{R}_D|\mathbf{O}|^2 + \mathbf{R}_D\mathbf{R}^*\mathbf{O} + \mathbf{R}_D\mathbf{R}\mathbf{O}^* \quad (6)$$

The initial two terms relate to the zeroth order of diffraction, while the third term represents the twin image, and the fourth denotes the real image. It's crucial that the value of θ is sufficiently large to distinguish between the real and twin images on the observation plane. Nonetheless, θ shouldn't surpass a specified limit to prevent the spatial frequency of the interferogram from exceeding the CCD's resolving capability. The wavefront Ψ at a distance d from the hologram plane can be derived using the Fresnel integral as cited in (Cuche et al., 1999b). The amplitude and phase images can be determined using $Re(\Psi)^2 + Im(\Psi)^2$ and $\arctan \left[\frac{Re(\Psi)}{Im(\Psi)} \right]$, respectively. The phase map is restricted to the $[-\pi, \pi]$ interval. Standard phase-unwrapping methods can resolve height differences greater than $\lambda/2$.

2.1.4 Focus distance

The bacteria studied in this thesis are considered 'phase objects'. That means that they mainly change the phase of the light that passes through. They have a negligible effect on the amplitude. In reconstruction distances close but outside the focus distance are amplitude variations close to the 'phase object'. These variations increasingly disperse the further apart the reconstruction distance is from the focus distance (Dubois et al., 2006).

2.1.5 Limitations

There are several inherent limitations to both DHM and QPI resulting in noisy images. These are temporal noise, spatial noise, optical noise and background noise.

Temporal phase noise, which refers to minute displacements between the object and the reference beam, originates from factors such as mechanical vibrations and fluctuations in the surrounding air.

Spatial noise, originates from debris within the measurement device or cell culture. This type of noise is hard to get rid of.

The main optical noise are speckles. Speckles are grainy patterns in the image caused by unwanted interference among light waves at the detector. High spatial and temporal coherence of incident light increases the prominence of speckle patterns (Park et al., 2018). To reduce speckles the following two methods can be used. The first method is spatial mitigation. This method scatters incident light in various directions using diffusers. By diversifying the directions of light propagation, spatial coherence is reduced, and speckles are mitigated. The second method is temporal mitigation. Temporal mitigation involves using light with a broad spectrum for illumination. A broad spectrum contains various wavelengths, decreasing the temporal coherence of light and thus reducing speckles (Park et al., 2018). It's worth noting that the light source used in this work exhibits high coherence, given its single-wavelength nature.

Both temporal and optical noise introduce random fluctuations in the images. To counteract this noise, multiple images can be averaged. Described by the central limit theorem, the random noise is reduced by the square root of the number of images averaged, as described

by the following equation:

$$\sigma(\bar{X}) = \frac{\sigma}{\sqrt{n}} \quad (7)$$

In this equation, $\sigma(\bar{X})$ denotes the standard deviation of the sample mean, σ stands for the standard deviation of the original population, n represents the sample size, and \bar{X} signifies the mean of the sample measurements.

2.1.6 Phase shift to cellular dry mass conversion

Barer proposed linking a cell's refractive index to its dry-mass density (Barer, 1952). This idea assumes that the refractive index is proportional to the cell's dry matter.

$$n_{cell} = n_{H2O} + \gamma\rho \quad (8)$$

where $\rho = M_{dry}/V_{cell}$ is the average dry matter concentration and γ is a constant known as the refraction increment. This value for γ is measured for individual constituents of the cell. An average of $\gamma = 0.175\text{ml/g}$ was found for *Escherichia coli* B/r strain grown in MM+glucose (Oldewurtel et al., 2021b).

Dry mass is then obtained from the integrated phase ϕ plus a correction due to the refractive index of the medium, n_{medium} , which is higher than the refractive index of water, n_{H2O} .

$$M_{dry} = \frac{1}{\gamma} \left[\frac{\lambda}{2\pi} \iint \phi(x, y) dx dy + V_{cell}(n_{medium} - n_{H2O}) \right] \quad (9)$$

where λ is the wavelength (Oldewurtel et al., 2021b).

2.2 Segmentation and tracking

Microbial dynamics play a crucial role in microbiological research. As our understanding of bacterial populations deepens, the need for rigorous data processing is evident. Modern research requires not only qualitative descriptions but also quantitative accuracy. In this context, bacterial segmentation and tracking become essential, providing a more refined approach to microbial systems. The automation of hardware and software enables researchers to generate huge datasets (Bakshi et al., 2021). With the increase in size, manual analysis is becoming both time-consuming and error-prone. Automated segmentation and tracking address these challenges by efficiently handling the increasing volume and complexity of data. Automated methods not only provide deeper insights but also offer cost and time savings.

2.2.1 Interactive learning and segmentation toolkit

lلاstik is a popular open-source tool for interactive image analysis (Berg et al., 2019). It provides a user-friendly graphical interface that allows users to perform several image analysis workflows. Data can be labelled directly in the image data, and then lلاstik offers instant

feedback, allowing users to see and refine their results quickly. Ilastik is used in various studies to label the training data semi automatically (Gabel, 2021; Lugagne et al., 2020; O'Connor et al., 2022). An expert trains the algorithm and then has to control and readjust the images. Pixel classification is the workflow to segment the images. It provides various generic pixel features, such as smoothed pixel intensity, edge filters and texture descriptors. Features can be manually selected, and parts of the image annotated. Based on the selected features and annotated data, a random forest classifier is trained. The results of this classifier are then shown live.

The basic workflows for segmentation in Ilastik only have a limited predetermined feature set. This makes it hard to generalize well for different experiments and other bacteria. Ilastik would offer the integration of more complex models such as neuronal networks. However, at the moment it is limited to a set of pretrained neuronal networks and does not allow retraining of the user. In the future this feature will be added.

2.2.2 Deep Learning for Time-lapse Analysis

Deep Learning for Time-Lapse Analysis, in short DeLTA, is a processing pipeline that automatically segments and tracks cell data. The first version of DeLTA was focused on the analysis of images from so-called "mother machine" microfluidic devices (Lugagne et al., 2020; Yang et al., 2018). In this device, bacteria are trapped in a one-ended growth chamber and progressively flushed out of the mother machines chambers.

The successor, DeLTA 2.0, is an extension to a two-dimensional growth environment (O'Connor et al., 2022). Both DeLTA and DeLTA 2.0 are based on a U-Net, a kind of convolutional neural network (CNN), architecture for segmentation and tracking. DeLTA 2.0 is available to download and already pre-trained on phase contrast images from various bacteria. DeLTA 2.0 offers the functionalities to easily retrain the U-Nets for new data. When doing so it is suggested to use the pre-trained parameters.

2.2.3 U-Net

The U-Net has shown to work very well in image segmentation (Ronneberger et al., 2015). Since its development in 2015 it has been used in various works in biological image processing. The Figure 2 shows the architecture of the U-Net. In the contracting pathway, convolutional layers capture local, high-resolution features, commonly referred to as "low-level" features. Subsequent pooling operations downsample these feature maps, facilitating the identification of increasingly abstract or "high-level" features as one moves deeper into the network.

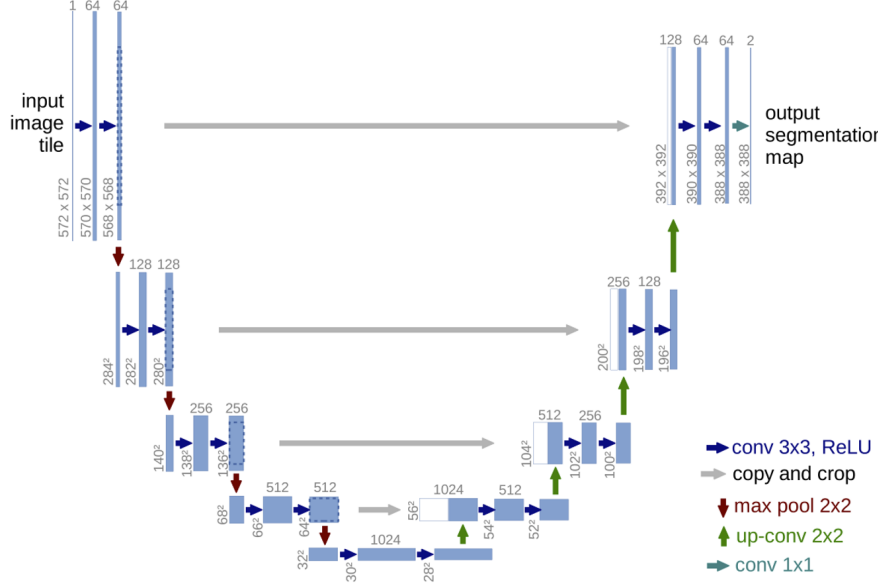


Figure 2: Architecture of the U-Net. The U-Net architecture first encodes the input images into high-level features (left side) and then decodes (right side) these features back into the original image resolution. Connections between the encoder and decoder paths preserve spatial information.

The expansive pathway serves to upsample these high-level features and concatenate them with their low-level counterparts from the contracting pathway. Additional convolutional layers in the expansive pathway allow multi-resolution feature integration. These layers are capable of learning composite features by combining information across different levels of abstraction and spatial resolution.

The expansive pathway is constructed to be largely symmetrical to the contracting pathway, contributing to the network's U-shaped architecture. This symmetry enables a balanced feature representation, by using both local and global contextual information in the final segmentation output. This dual-pathway structure, represents a methodological extension to the "Fully Convolutional Networks for Semantic Segmentation", from which the U-Net architecture is based on (Shelhamer et al., 2017).

3 Material and methods

3.1 From hologram to a clean phase image

The pipeline starts with holograms generated by the DHM setup and proceeds to generate refined phase images. This process entails several key steps: phase image construction, surface plane subtraction, focusing, background subtraction, and finally, spatial averaging.

3.1.1 Construction of the phase image

The image pipeline starts with images of an experiment taken with a DHM setup from LyncéeTec. These images are 32Bit, 1024x1024 pixels intensity inference images taken with a CCD camera. LyncéeTec provides a software, called Koala, for processing the inference images. When working with DHM, understanding the reconstruction distance is crucial. Koala can take a DHM inference image, often referred to as a hologram, and reconstruct it into a complex image. This complex image represents the objective beam propagated back to the specified reconstruction distance.

The critical aspect here is that the observed object will be in focus if it aligns with the designated focus distance. Objects located further from this distance will have increasingly dispersed signals. Through continuous reconstruction, multiple objects can be brought into focus, corresponding to their respective positions in the depth. This enables three-dimensional tracking and creates the illusion of a three-dimensional image. The reconstructed images, while providing the illusion of three-dimensionality, inherently include the dispersed signal from objects at varying focus distances, making them not truly three-dimensional representations.

In off-axis DHM, the in-focus image is shifted to the side of the Fourier-transformed image. This shift effectively isolates a specific part of the image, which contains higher spatial frequencies. By focusing on these higher frequencies, the method enhances certain image details, but it can also reduce the overall size of the output image. This reduction in size is the reason why the complex output image is decreased to 800x800 pixels in dimensions.

This complex image can be separated into an amplitude image and a phase image. Since the bacteria observed are phase objects the amplitude image does not hold any information if the bacteria are in focus. The main interest is the phase image.

3.1.2 Surface plane subtraction

Looking at multiple phase images shows that the plane, on which the objects lie, is not always flat. In some images there is only a tilt, while in more distorted images the plane is curved. This uneven surface stems from imperfect alignment of the optical instruments in the DHM setup. To flatten the phase image a plane, based on the polynomial features of the pixel coordinates, is subtracted. To calculate this plane, first a polynomial feature expansion is done, which for the example of a second degree polynomial are the features $[1, x, y, x^2, x * y, y^2]$. The values for each pixel are calculated and written into a matrix X . The plane is then calculated by

using the closed form solution of the ordinary least squares estimator $\hat{\beta}$. Using this estimator the least squares solution for the plane \hat{y} can be calculated.

$$\hat{\beta} = (X^T X)^{-1} X^T y \quad (10)$$

$$\hat{y} = X \hat{\beta} \quad (11)$$

where y is the dependent variable, so in this case the pixel values of the image. Calculating the inverse takes considerable time since it generally scales with $\mathcal{O}(n^3)$. In this case n corresponds to the number of pixels in the image. Since the plane is calculated often with different images the computational time accumulates.

But the knowledge that X corresponds to the pixel coordinates, and thus stays constant for any image of the same size, can be used. $(X^T X)^{-1} X^T$, the so called "Moore-Penrose pseudoinverse" needs only be computed once. This significantly decreases the computation time.

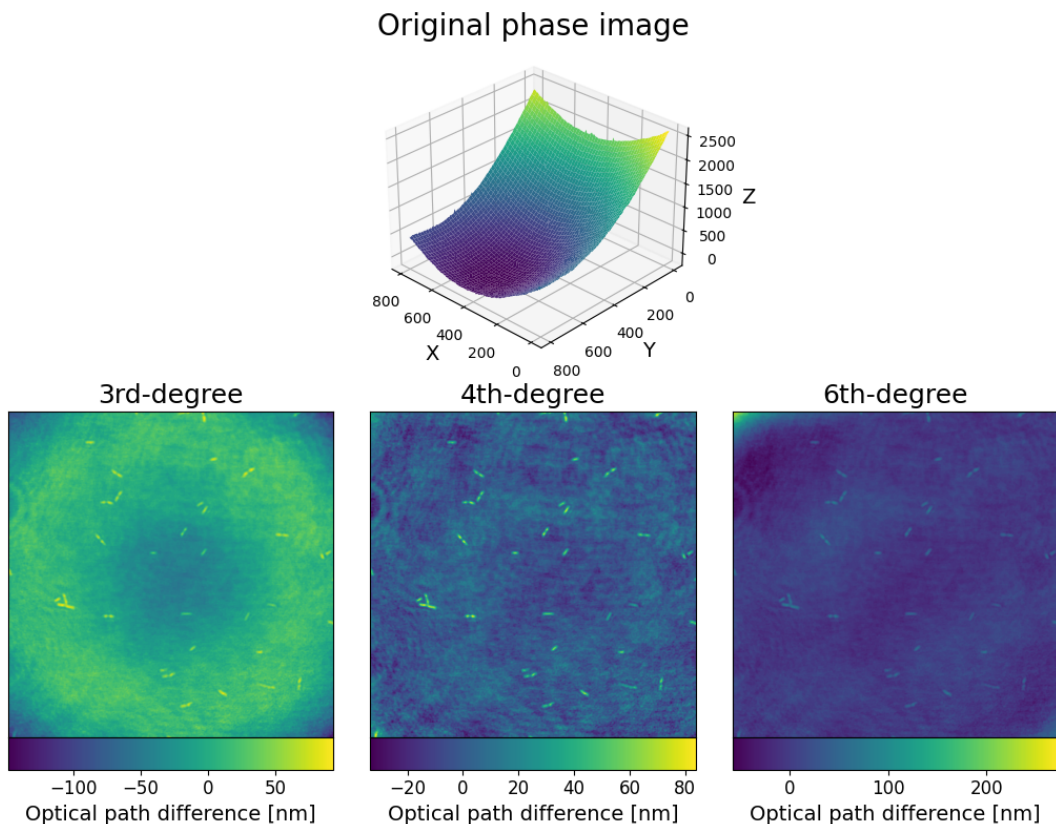


Figure 3: Fitting a polynomial curve to the reconstructed phase image. Top: Plane is distorted both radially and axially resulting in a warped and tilted surface. Bottom: Different degrees of plane fitting lead to different results. Low degree planes underfit the background, while to high degree planes overfit the data.

The curvature of the phase image presented in Figure 3 presents an extreme scenario in terms of both magnitude and the shape of the curve. In the original image (top), the phase shifts

attributable to bacteria are not discernible, given that the curvature is beyond an order of magnitude larger.

The image on the bottom left of Figure 3 demonstrates that a third-degree polynomial plane insufficiently approximates the image, as the general contour of the underlying plane remains visible. Subtraction of a fourth-degree plane yields a flat image, which is the desired outcome shown in the second accompanying figure. The same holds true when a fifth-degree plane is subtracted from the image.

However, the introduction of a sixth-degree plane results in overfitting the image, as evidenced by the loss of flatness at the peripheries shown by the last image in the figure. In terms of a two-dimensional input, the sixth-degree polynomial plane carries 28 features.

3.1.3 Focusing

For this work the objects of interest, namely the bacteria, are found at the border between the substrate and the glass, thus only one reconstruction distance is of interest. In this reconstruction distance all bacteria are in focus. Generally, the reconstruction distance, where the bacteria are in focus, is fixed and therefore the same for all images. However, sometimes this is inconsistent and the focus distance can vary significantly. A possible reason is that the perfect focus system of the microscope does not readjust fast enough. In these cases, using the set reconstruction distance, results in the bacteria being out of focus. That is why a method for focusing, based on the image's features, is used.

In Figure 4 are two *Escherichia coli* bacteria at various reconstruction distances. It is known that bacteria are phase objects, meaning that they barely change the amplitude of passing light, but they change the phase significantly. So for the image to be in focus this needs to be accounted for.

In this figure several observations can be made that are generally true. Slightly below the focus distance, destructive interference causes a reduction in amplitude at the location of the bacteria, whereas above the focus distance, constructive interference enhances the amplitude. As you move further away from the focus distance, these effects become more dispersed.

At the exact focus distance, the phase image accurately represents the thickness of the bacteria. However, as you move away from this focus distance, the phase differences become less clear. The phase information disperses, and just slightly below the focus distance, you may observe a phase image with a more pronounced and sharper peak in the middle of the bacteria.

The observations lead to the following conclusions. Far away from the focus distance, the bacteria in both the amplitude and the phase image are dispersed. Close to the focus point the bacteria are well visible in the phase image. The bacteria is only invisible at the exact focus distance, a slight deviation results in either low or high amplitude.

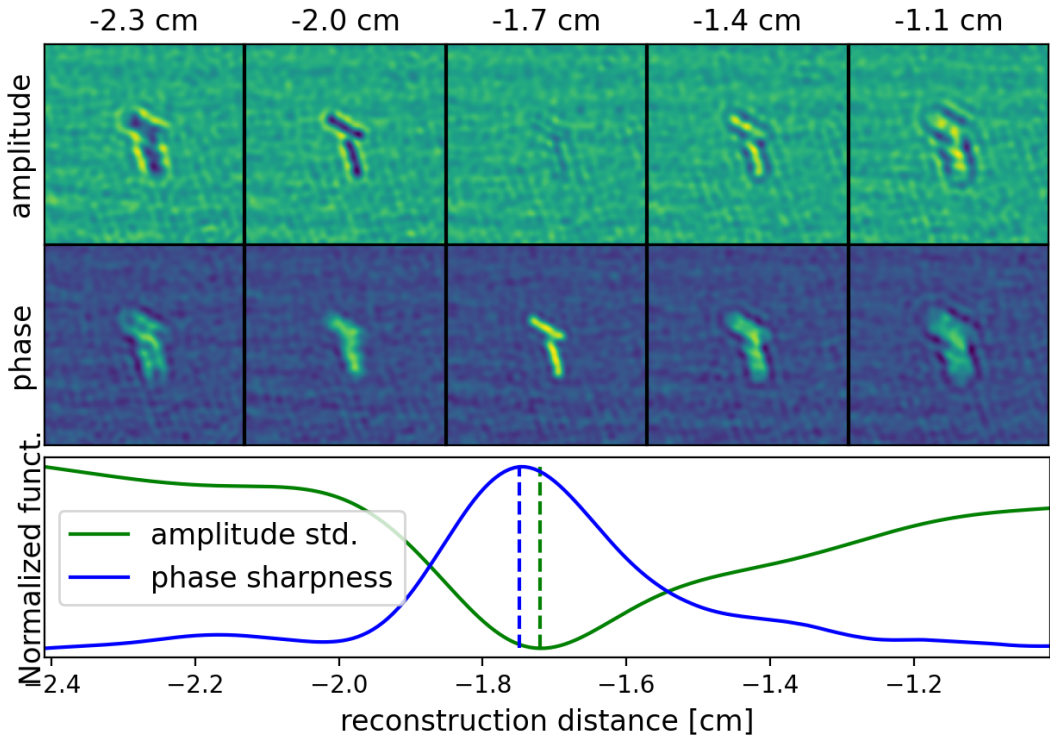


Figure 4: Image evaluations at various reconstruction distances. While five images are presented here, the underlying functions are derived from a much finer spacing. The functions are based on the images features. The images align with the function represented below. In the image in focus the bacteria are not visible in the amplitude image and sharp in the phase image. The dotted lines represent the reconstruction distance where the functions are minimal respectively maximal.

These observations lead to the following algorithm to find the focus distance:

1. Find the focus region by maximizing the sharpness in the phase image.
2. Find the exact focus distance by minimizing the standard deviation in the amplitude image.

To calculate the sharpness the phase image is first clipped at zero, since strong negative values can not stem from bacteria and would only disturb the result. Then the sharpness is calculated with the following equation:

$$f_{\text{sharp}}(d) = \sigma \left\{ [\nabla_x \Phi(d)]^4 + [\nabla_y \Phi(d)]^4 \right\} \quad (12)$$

where d is the reconstruction distance, σ is the standard deviation and Φ is the phase image. The exact minimum is found by a grid search with progressively finer grid size. Various other minimization techniques were investigated but this proved the fastest and most reliable. Calculating the phase image at a certain distance involves the steps described in previous chapters, namely image propagation and surface plane subtraction. Since focusing needs around 30 function evaluations it's very important that the previous processes are fast.

Leveraging the power of the computer's GPU, Koala's image propagation only takes $\sim 20\text{ms}$. However, Koala fails to efficiently clear all cached data during operation, leading to a gradual slowdown. The only solution that could be found was to periodically close and open Koala. This has been automated but the automation needs a graphical user interface. Therefore, the monitor of the computer that the program is running on needs to be on at all times.

The trick of storing the Moore-Penrose pseudoinverse decreases the surface plane subtraction from $\sim 600\text{ms}$ to $\sim 20\text{ms}$. Calculating the phase sharpness or amplitude variation takes around 10ms. So the overall focusing method takes about 1.5s per image.

3.1.4 Background subtraction and spatial averaging

In an experiment different positions of the sample are looked at over time. At each of these positions 25 images are recorded. These images are shifted by approximately $2\mu\text{m}$ into a 5×5 grid. Each image recorded has a sidelength of $100\mu\text{m}$, so most of the recorded images are overlapping.

To isolate the background noise, which represents the signal from particles on the DHM instruments, we take advantage of its consistent position across the images. The background noise remains static and does not shift with the images. It is therefore isolated by taking the median of all images. The median is used since it is robust to outliers, which in this case are bacteria. This is done only for the first ten timesteps, in later timesteps the average of the first ten images is used. The reasoning is that the background does not change significantly with time, but the calculation of the background gets harder, since the images get fuller with bacteria.

After the subtraction of the background the images are aligned. The exact shift between each image is calculated by cross correlation. These aligned images are then averaged into a single image. This decreases the random noise from speckles and vibrations by the square root of the number of averaged images, which can be seen in Figure 5.

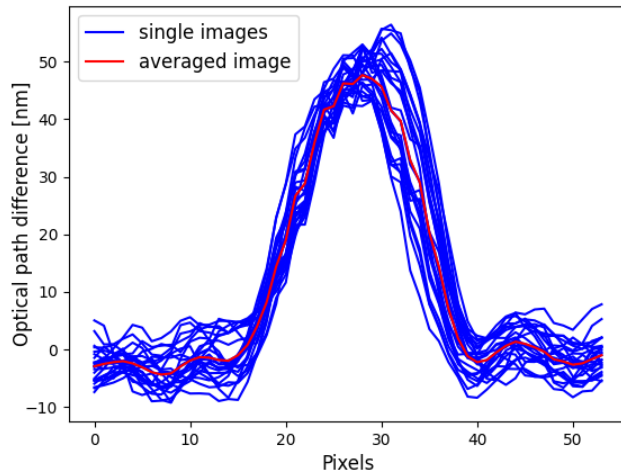


Figure 5: Line through the bacteria of all aligned images and the spatially averaged image. Averaged line is much less noisy compared to the single lines.

3.2 Bacteria segmentation and lineage tracking

DHM holograms of a position in the experiment sample are taken periodically. These holograms are processed as described in subsection 3.1.1 and combined to a time-lapse sequence. For segmentation and lineage tracking, we employ DeLTA, a neural network-based image pipeline that requires training data. The generation of this training data is achieved through the use of Ilastik.

3.2.1 Preparing training data with Ilastik

Ilastik is a powerful tool that utilizes machine learning algorithms to perform various tasks such as segmenting, classifying, tracking, and counting cells or experimental data. Its user-friendly graphical interface enables interactive learning, making it easier to work with large datasets. Additionally, Ilastik offers multiple workflows to suit different needs and applications, such as pixel classification and pixel tracking, which were utilized in this particular work. The main file formats used by Ilastik are HDF5 and N5. Phase images were changed into HDF5 time series.

The phase images of one, or several positions are loaded as time series data into the pixel classification workflow. Here individual pixels are labeled by hand. Ilastik augments the original image, resulting in a set of features which are then used to predict each pixel's label. Ilastik calculates the label's probability for each pixel, maximizing the matching.

The goal of this classification is twofold. Firstly, the bacteria need to be separated from the background and secondly individual bacteria need to be separated from each other. This is tricky because sometimes there is no room between them and thus detecting the boundaries is hard. To solve this problem several labels are used. The manual classification is shown in the Figure 6.

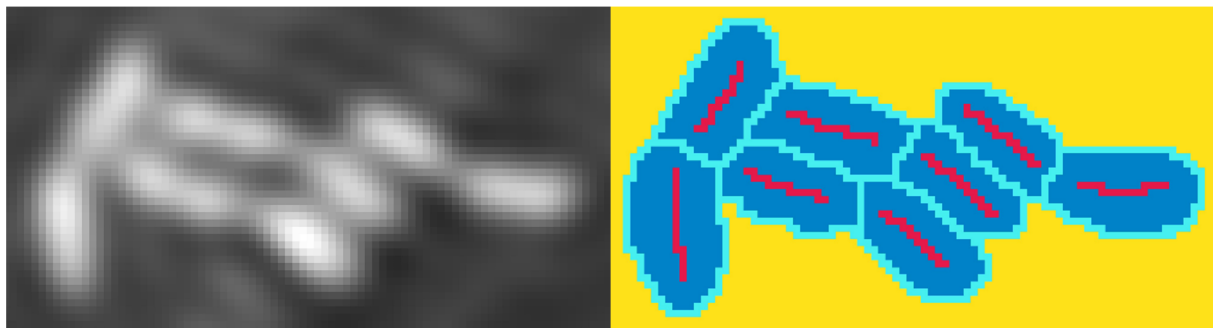


Figure 6: Manual pixel classification into core (red), main bacteria (dark blue), boundary (light blue) and background (yellow)

The image is labeled with the following four classes: The background is yellow, the bacteria's boundary is light blue, its inside dark blue and the core of each bacteria is red. The core is a strip in the middle of the bacteria along its length. It is a strip with minimum width to

maximize the distance to other bacteria's core that are side by side to each other. Separation between the background and each bacteria would be possible without the light blue boundary, but it would not be clear where they are separated. This label decreases the probability of the dark blue label and thus make a natural boundary at the right place.

Manual labeling is a tedious work that takes a long time. To make sure the algorithm also works well with a limited amount of training pixels, the feature set can be reduced. This avoids the problem of overfitting. Ilastik provides the option "Suggest Features" to find the most influential features. Using around 11 features seemed to be the best compromise between accuracy and simplicity.

After some of the data is labeled the rest can be calculated by pressing the "Live Update" button. This updates the rest of the images. They can be checked for correctness. If they are not yet good enough more pixels can be labeled. The output of the pixel classification workflow are probabilities for each pixel and class.

Both the phase image time series and pixel predictions are then loaded into the next workflow, namely pixel tracking. In the first process the individual bacteria are segmented. To do so the hysteresis thresholding technique is utilized. This two-step approach begins by identifying the object cores, and then broadens the criteria to capture the complete object. Within the interactive graphical user interface, the operator has the flexibility to specify the probability threshold for identifying the cores. Setting this value too low results in ineffective separation of bacteria, and conversely, high values separate each bacteria into several. Probability ranges of 20% to 25% for the core, and 40% to 50% for the full bacteria were found to work best. The resulting object classification can be interactively checked and should ideally look similar to Figure 7.

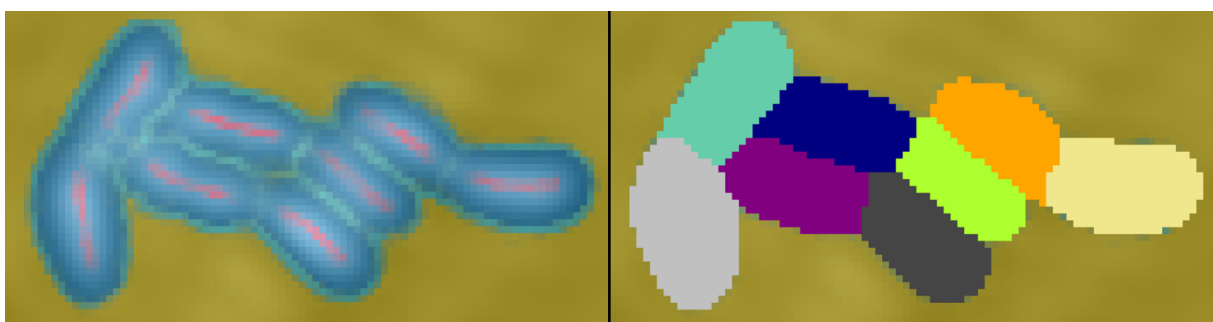


Figure 7: Ilastik's object detection. Bacteria are separated by the red core pixels. Size of the bacteria is determined by the dark blue main bacteria pixels.

In the next steps, we need to correctly mark where the bacteria divide and remove any wrongly marked objects. After that, we move on to the tracking part. Here, you can pick settings to help track the bacteria better. The main settings you can change are how much it costs for bacteria to appear or move. But since bacteria don't usually just pop up or move a lot, you usually don't need to change these settings.

There are different ways to export the tracking results. The CSV file was chosen since it was the most straight forward.

3.2.2 DeLTA: segmentation and tracking

DeLTA (Deep Learning for Time-lapse Analysis) is a system that uses U-Nets for both segmentation and tracking of objects. While it's mainly designed for phase contrast images, it needs some tweaks to work well with quantitative phase images.

Firstly, DeLTA can't handle negative values. All images are usually treated as unsigned integers with a bit size of 16 per pixel. So, we adjust all phase images to fit into this range. Specifically, we map values from $[-\pi, \pi]$ to $[0, 65535]$.

Secondly, the name of each image needs to include three key details: position, channel, and frame (or timestep). The position and timestep are already part of the phase images, but the channel is new. This extra detail lets us add other types of images, like fluorescence images, into the mix. These images are not used for segmentation or tracking but they can be used to calculate cell features afterwards.

In the training images created by Ilastik, bacteria cells are touching each other. DeLTA, however, needs empty space between cells because it simply identifies something as either a cell or not a cell. To fix this, the original DeLTA study made cells appear a bit smaller than they actually are. They also emphasized the importance of the empty spaces between cells by increasing these pixel weights (O'Connor et al., 2022). Pixel weights are used to assign varying degrees of importance to individual pixels, allowing the model to highlight or de-emphasize certain regions or pixels during the learning process.

This approach doesn't work as well for quantitative phase images, where cell borders are fuzzy and cells are closely packed. In such cases, even a few wrongly labeled pixels could blend two distinct cells into one. But there's a benefit to using quantitative phase images: it's easy to tell the background from cells. It is possible to only segment the core of each cell, keeping the distance between the cells as big as possible. After running DeLTA, the cell sizes are then gradually expanded until they cover the real cell area. This is a technique similar to water shedding.

The pixel weights are selected to address three key issues. First, there should be a smooth transition, meaning pixels clearly in the core shouldn't be mislabeled, and the same goes for pixels at the far edges or boundaries. Second, pixels between bacteria are more crucial to label correctly than those further away. Finally, since the cores make up a small portion of the image, they need extra weight. This ensures that the program doesn't mistakenly identify all pixels as non-cells.

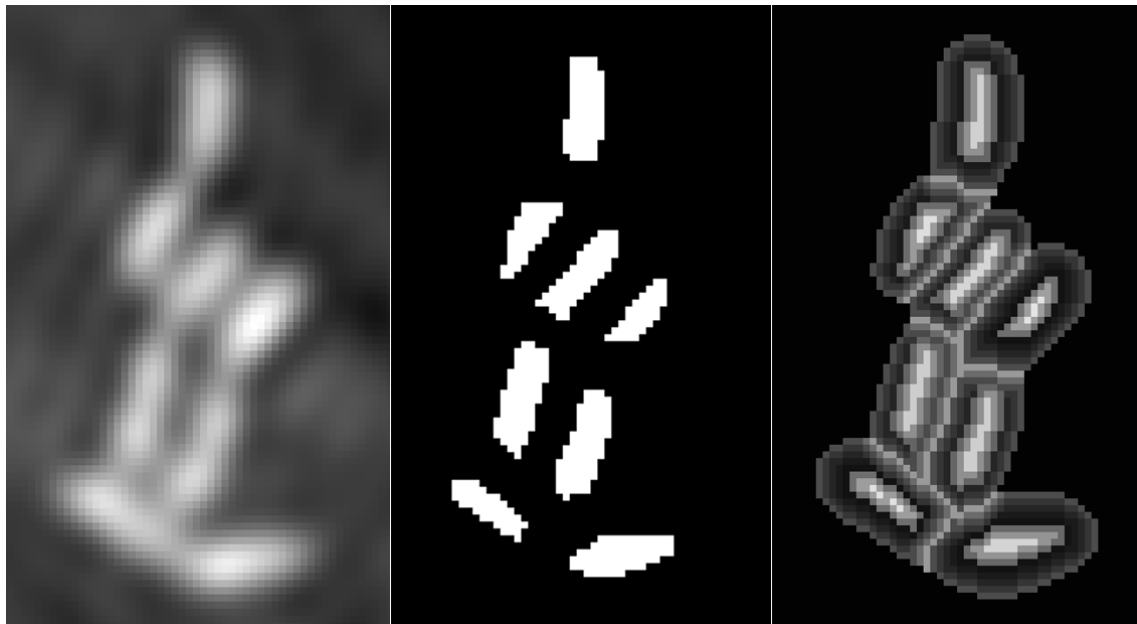


Figure 8: DeLTA's segmentation and pixel weighting. Original image (left), the segmentation (middle) and pixel weighting (right) are shown. Bacteria's are reduced to the core to ensure separation. Boundary has increased weights and boundary between bacteria even more. Bacteria's separated cores have higher values and increasing to the middle.

Tracking cells is straightforward when they aren't moving. The same method used for Delta phase contrast images can be applied here. For tracking, the U-Net model takes four inputs: the previous image, its segmentation, the current image, and its segmentation. It also needs information about the cell that was being tracked previously.

The U-Net's job is to locate the current cell that is being tracked. It must also determine if the cell has divided into two. To do this effectively, the model gives more importance to pixels near the tracked cell compared to those farther away. Additionally, pixels belonging to the cell being tracked are considered more important than those that are not part of the tracked cell. The training data produced as described before is then augmented. Training data augmentation is an integral part for the U-Net and thus also following DeLTA. This allows the network to learn invariance to such deformations and increase the robustness of the network. The value of data augmentation for learning invariance has been shown in the scope of unsupervised feature learning (Dosovitskiy et al., 2016). Training images are rotated, horizontally and vertically flipped. Furthermore, Gaussian noise, Gaussian blur, and elastic deformation are added.

4 Results

The DHM pipeline can convert holograms into focused phase images and further reduce its noise level by spatially averaging them. Time-lapse phase images are then analysed with the help of DeLTA to segment and track the bacteria lineage. The bacteria's features, such as length, width and mass, are easily accessible.

4.1 Phase image construction

In this section, the phase image is created. Koala is used to reconstruct single phase images, but these images still have a lot of noise. The goal is to reduce this noise while keeping the original signal intact. To assess improvements, we look at the background areas where no bacteria are present; the phase value should ideally be zero in these regions. An exception is the improvements due to focusing; nearly all the change is in areas with bacteria. Here, the image in focus is assumed to be the ground truth. The analysis is based on 64 images from two separate experiments. Each of these images consists of 25 sub-images, with a total of 1600 sub-images examined. This large sample size ensures that our results are robust despite potential variations in error.

4.1.1 Surface plane Subtraction

The reconstructed phase images are often on an uneven surface. It is created by the imperfect alignment of the optical instruments in DHM. The uneven surface can be a slight tilt but is often a more complex plane. The plane is calculated by linear regression on the polynomial features up to the fourth degree of the pixel coordinates. This plane subtraction can efficiently flatten the phase image, and an example of this improvement can be seen in Figure 9.

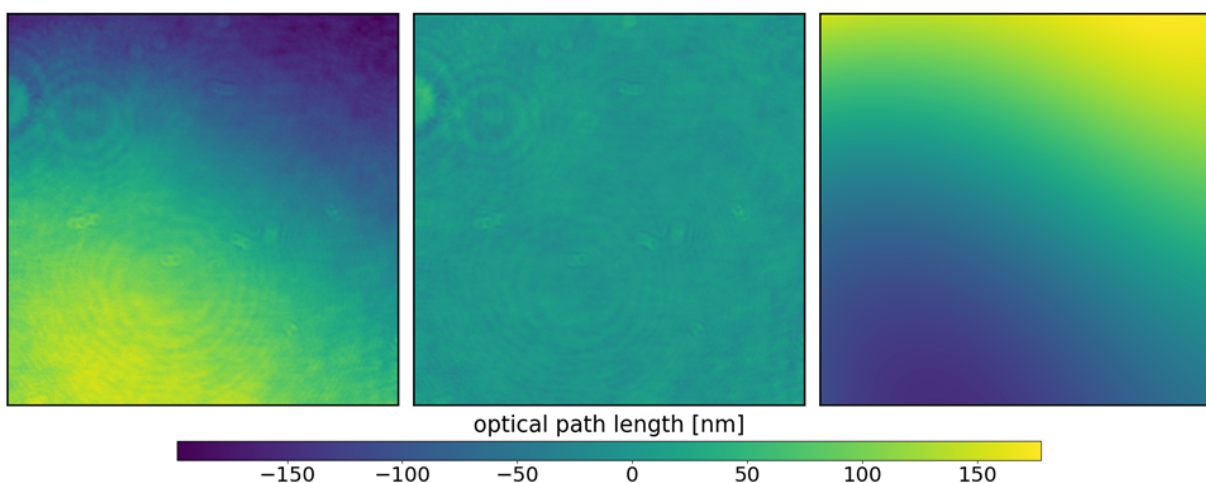


Figure 9: The images before (left) and after (middle) the surface plane subtraction, as well as the difference (right), are shown.

4.1.2 Focusing

Most images have a true focus distance very close to the set focus distance of the experiment, but some deviate significantly. The true focus distance is calculated with the method described in a subsection 3.1.3. At a reconstruction distance deviation from the focus distance of 0.2cm it becomes apparent by eye that the image is off focus. In the Figure 10 it can be seen that the bacteria in the unfocused image are very dispersed, whereas in the focused image, they are sharp.

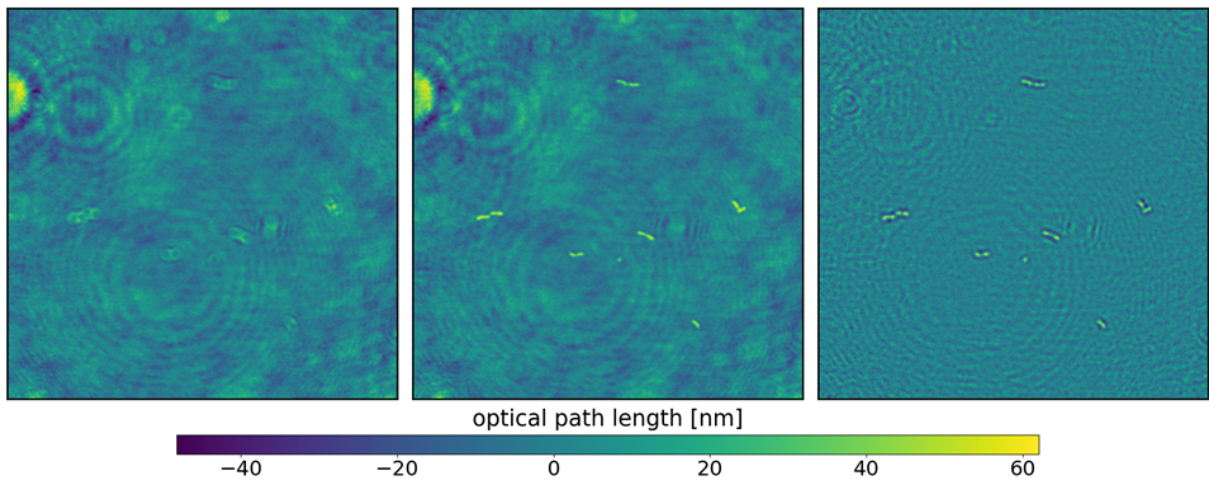


Figure 10: The images before (left) and after (middle) focusing, as well as the difference (right), are shown. This image is one of few significantly out-of-focus images. It has a focus distance of -1.49cm instead of the usual -2.3cm .

4.1.3 Background Subtraction

Particles on the optical instruments of the DHM cause the background noise. Because this noise is static, it can be isolated by taking the mean of the unaligned images. Most of the background does not have any pronounced areas, similar to Figure 11, but nonetheless, the noise is consistent, so subtracting it is worthwhile.

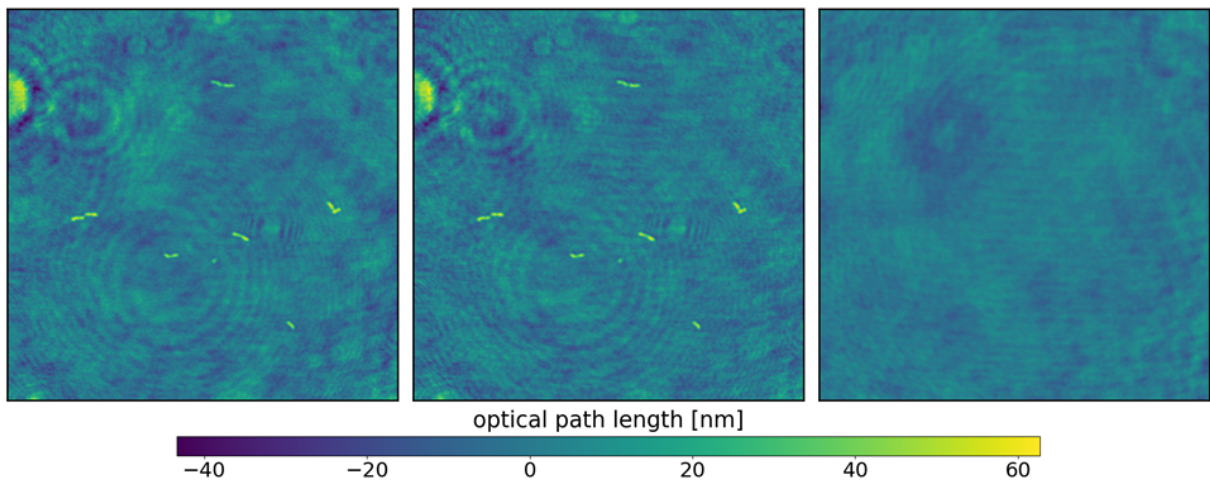


Figure 11: The images before (left) and after (middle) background subtraction, as well as the difference (right), are shown.

4.1.4 Spatial averaging

The 25 slightly shifted images are aligned, averaged, and sides are cropped. This decreases the random noise considerably. Most of the noise still in the images is spatial noise. It stems from disturbances with different depths. In images outside their reconstruction distance, they leave radial noise, which is hard to eliminate. Both these points can be well seen in Figure 12.

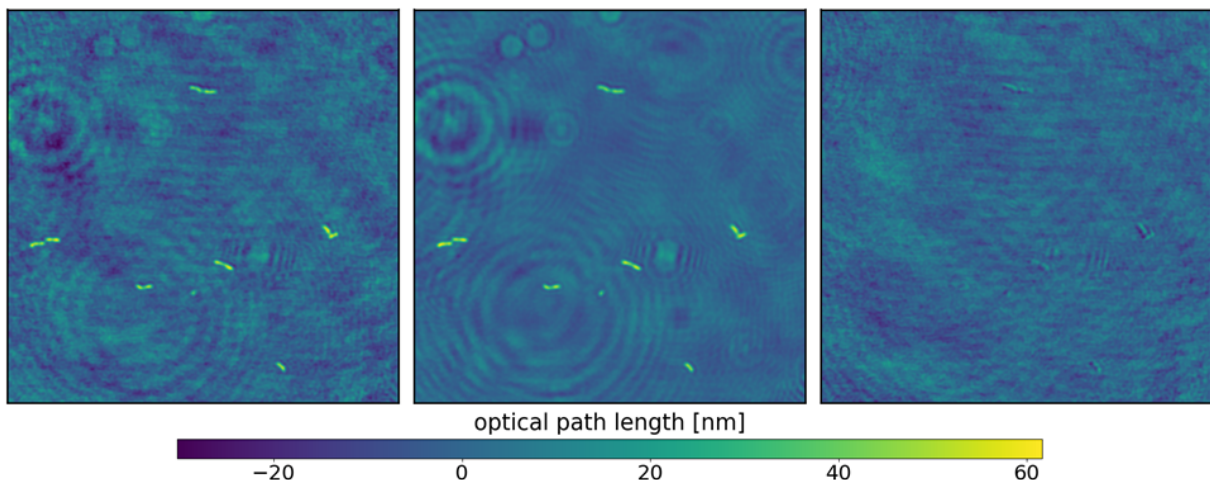


Figure 12: The images before (left) and after (middle) spatial averaging as well as the difference (right) are shown. Spatial averaging reduces random noise and thus smooths out the image.

4.1.5 Overall Improvements: pixel errors

These images do not have a ground truth against which they can be compared. What is known is that at places where there are no bacteria, the optical path difference should be zero. Since all processes, except for focusing, operate independently of bacteria, they should perform equally well on bacteria-free areas. We measure errors at locations devoid of bacteria to assess their accuracy. Focusing primarily affects bacteria, and since there is no established ground truth, the in-focus image is considered the reference point, comparing it to the out-of-focus images. It is assumed that the focusing noise is independent and additive to the other noise types, so the total mean (μ_{total}) and standard deviation (σ_{total}) are calculated by using the formulas $\mu_{\text{total}} = \mu_a + \mu_b$ and $\sigma_{\text{total}} = \sqrt{\sigma_a^2 + \sigma_b^2}$, where μ is the mean and σ is the standard deviation.

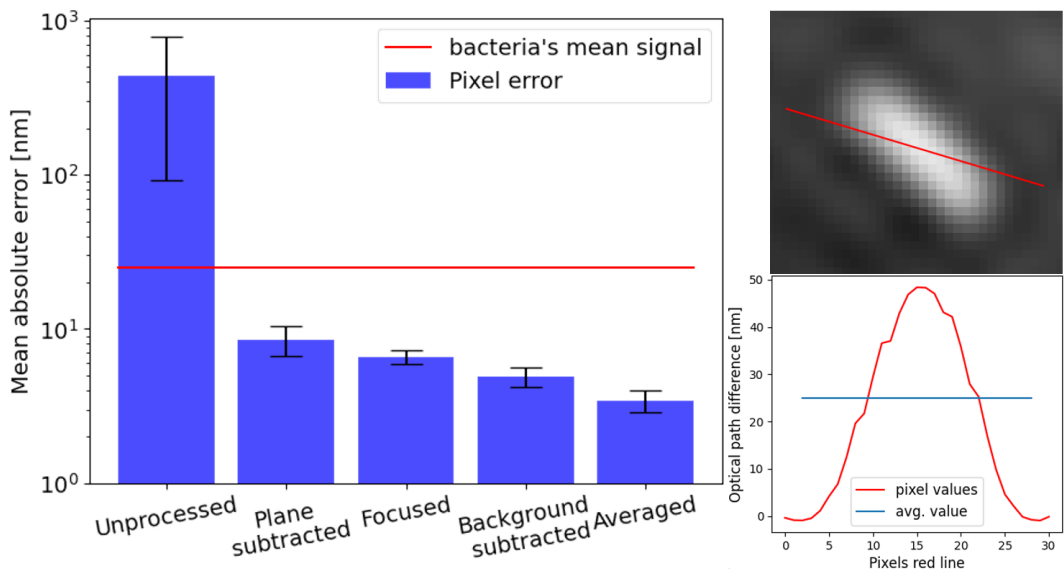


Figure 13: The pixel error is measured to track the improvements done by the processes. As a reference, a bacteria has a mean optical path difference signal of ~ 25 nm. The images on the right show a line through the bacteria and its corresponding optical path differences.

4.1.6 Focusing effect on bacteria's mass

If an image is out of focus, the phase difference is dispersed outwards. This has a detrimental effect. If the image is too much out of focus, calculating the shift to the other images can be impossible. But even if the shift is calculated perfectly, the out-of-focus image has a negative effect on the mass calculations. It can be assumed that a few out-of-focus images do not increase the segmentation size of the image as they don't have a visible impact. However, since the phase difference is dispersed, the phase difference is smaller in the segmented bacteria than it should be. Figure 14 shows a linear decrease in the bacteria's mass. For each image out-of-focus by 1cm, the averaged image decreases by approximately 3%. 1cm is a high but reasonable estimate for significantly out-of-focus images.

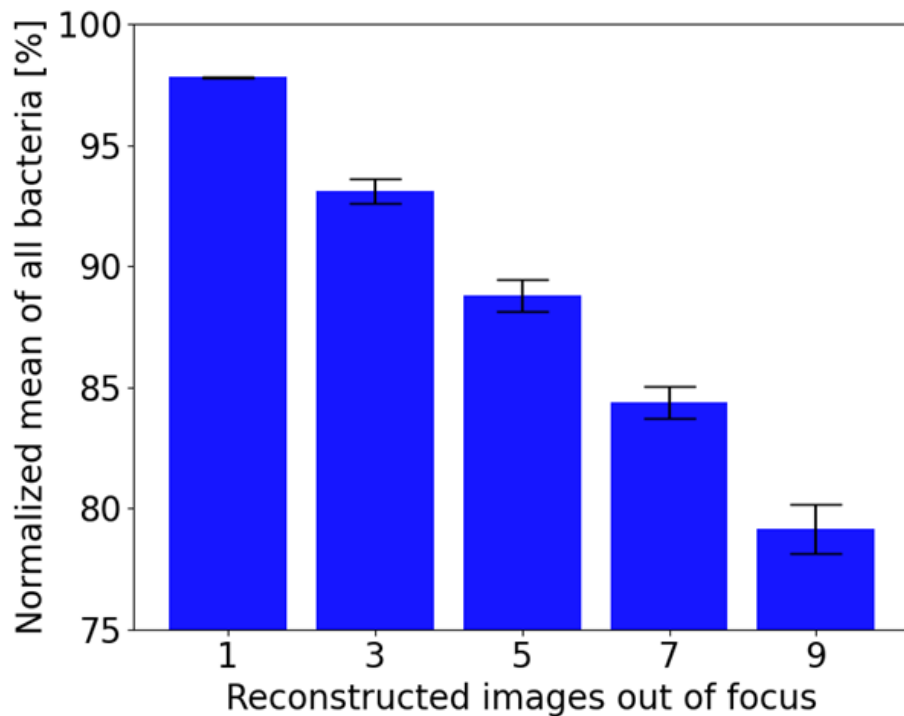


Figure 14: The plot shows the bacteria's mass decrease due to some images out-of-focus. The out-of-focus images are reconstructed at 1cm above the focus distance. Twenty-five images are used to calculate the average image.

4.2 Segmentation and tracking with DeLTA

The DeLTA pipeline is trained and tested with images produced with Ilastik as described in material and methods. Training images are produced from two different strains of bacteria; one strain has 344 images, and the other one has 980 images. The pipeline should be able to handle a new type of bacteria. That is why only the strain with 980 images is used to train, whereas the second strain is used for validation.

In a first step, the hyperparameters for the data augmentation were evaluated using a grid search. The tunable hyperparameters for data augmentation are Gaussian noise, Gaussian blur and the sigma value for elastic deformation. The U-Net needs to be trained for each test, which takes a lot of time. That is why Gaussian blur and noise were not tested independently. The highest amount of augmentation achieved the best result but by a low margin. The results can be seen in Figure 15.

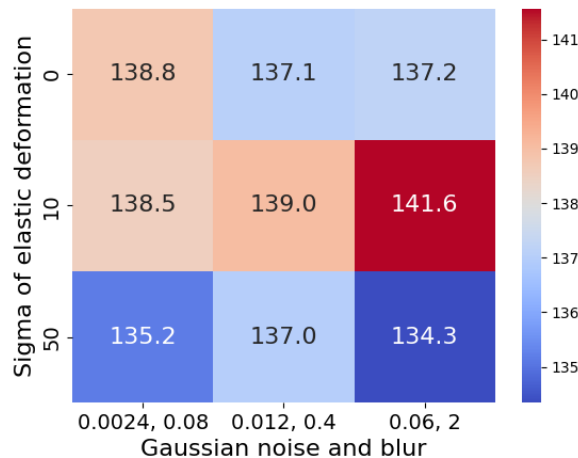


Figure 15: The hyperparameters for data augmentation are found by a grid search of various possibilities. The results are pixel-wise weighted binary cross-entropy of the validation data. Lower scores are better. High augmentation performed best, but not by a big margin.

The goal was to converge as fast as possible to find the best hyperparameters, so a high amount of training steps (1000) were used per epoch. That increased the training time in relation to the validation time. Like this, it took only ~ 22 epochs to find the best validation loss. A patience of 25 was used.

A lower number of training steps (50) was used to show the training process. The validation steps were not lowered from 300 since the prediction difficulty varies greatly depending on the image tested. This can be seen in the training history. The training loss has a much higher variance than the validation loss since it depends on fewer images. It can further be seen in the low correlation coefficient between them.

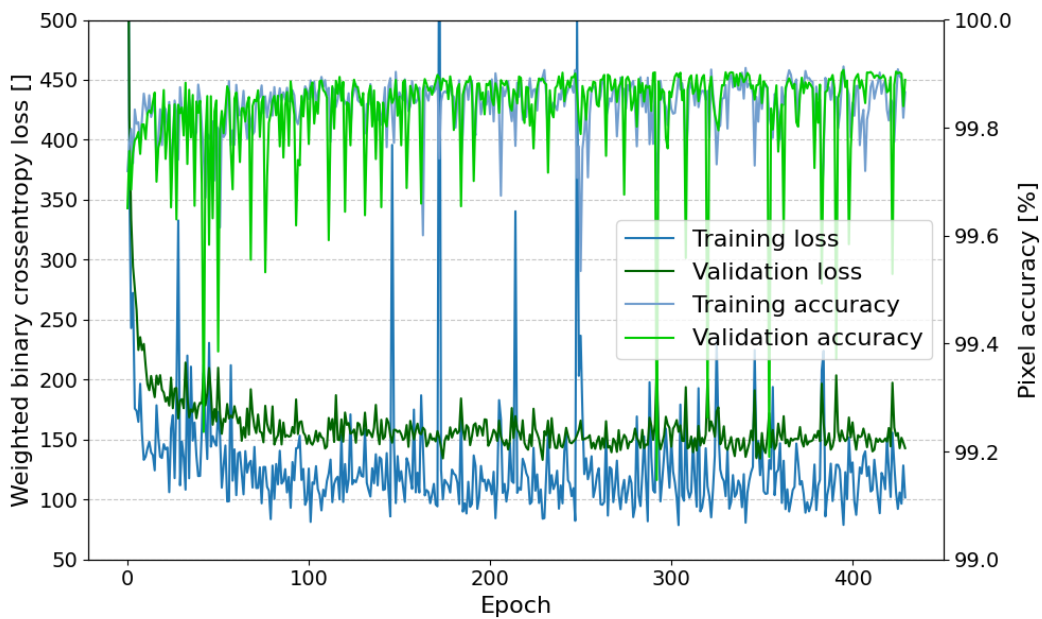


Figure 16: The training history for the segmentation U-Net shows fast improvements. After the first 100 epochs, the Net does not improve anymore. Fluctuations are high, indicating that some images are much harder to predict than others.

Training the U-Net for tracking is done the same way. The tracking problem is not complicated and DeLTA has near-perfect tracking after training.

The segmentation and tracking works mostly fine. There are some issues when bacteria are close to each other as seen in Figure 17.

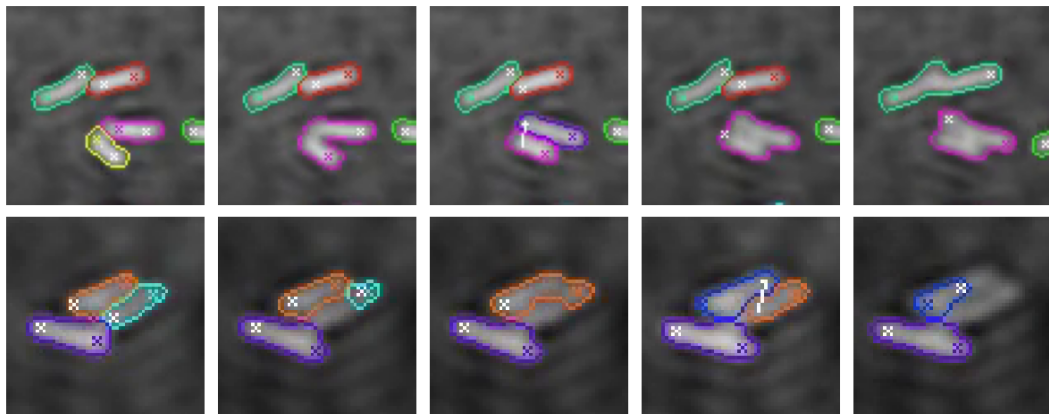


Figure 17: Images show errors in segmentation. Five consecutive timesteps are shown for two different challenging positions. It can happen, that close bacteria either merge or are not properly recognised.

4.3 Cell cycles

This pipeline will be used to evaluate the cell cycles of bacteria. This can be easily done with the output of the pipeline. Since DeLTA does not work perfectly, implausible cell cycles are sorted out. Reasons for being filtered out are the following:

1. No mother cell: cell cycles with no split at the start. Because they are initial cells, they emerge suddenly or their segmentation or tracking is faulty.
2. No split: cells cycles with no split at the end. Because they are at the end of the time-lapse, they disappear or their segmentation or tracking is faulty.
3. Extreme growth: cell growth between consecutive time steps exceeding 1.3 times its previous mass, or falling short of 0.9 times its previous mass.
4. Overall growth abnormalities: more than 3 times or less than 1.5 times the starting mass before dividing the second time.
5. Excessive movement: movement above $1.3\mu\text{m}$ between images indicates tracking errors

The mass growth of these types of implausible cell cycles are shown in Figure 18.

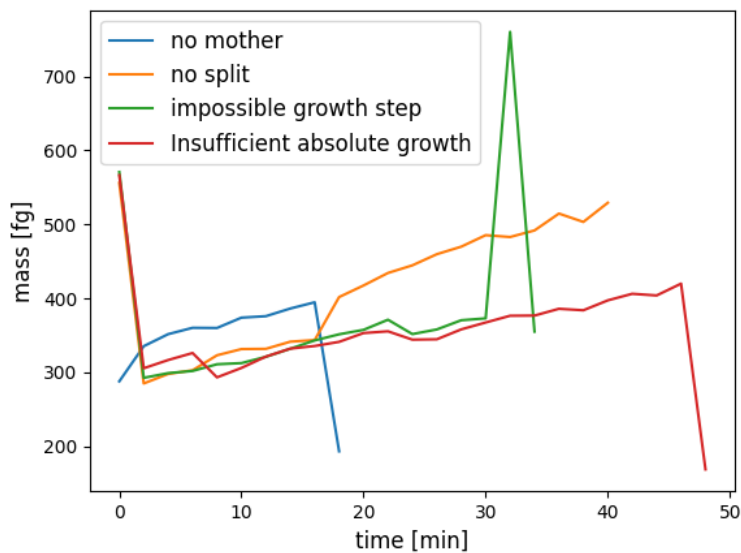


Figure 18: The mass growth of the filtered implausible cell cycles are shown in this figure.

Figure 19 shows a few of many valid cell cycles. These are the main result of the pipeline.

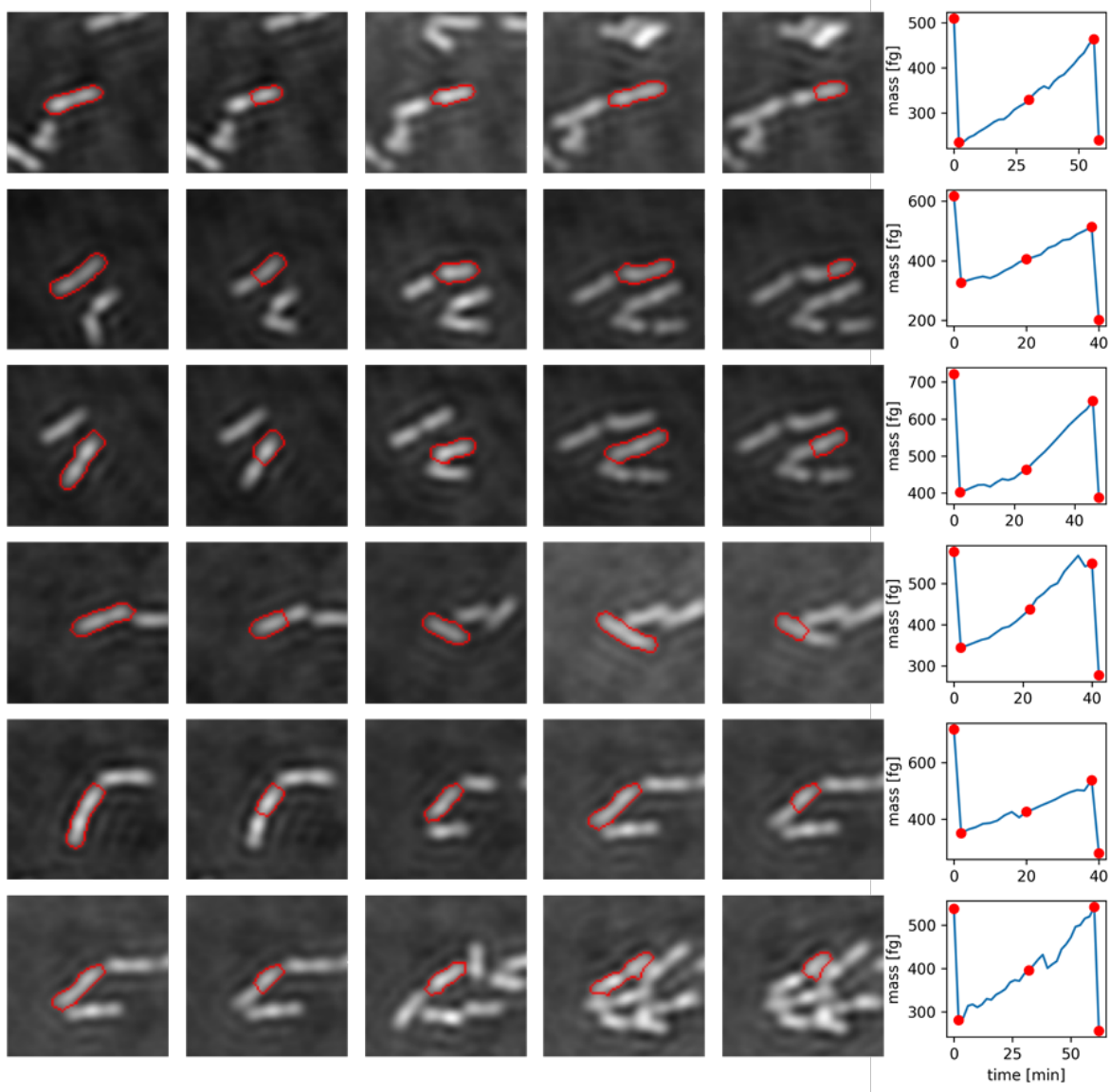


Figure 19: The plot shows the dry mass growth of various cell cycles. Each row shows one bacterial cell cycle. The first image is before and the second after the first split. The third is in the middle of the cell cycle. The fourth is before and the fifth is after the second split.

5 Discussion

5.1 Phase image

It has been shown that post-processing of the reconstructed phase image from DHM is paramount. The most important cleaning process is subtracting the surface plane. The size and shape of the surface plane varies a lot between the experiments, some are only tilting, whereas others have round shapes. The shapes inside one experiment are generally similar. Whether most of the true focus points are close to the set point or not depends heavily on the experiment. As shown in subsection 4.1.6, that focus-point-offsets have a big effect on the bacteria's mean optical path difference and thus on its mass. Additionally, it introduces noise and diffuses the bacteria's borders, making segmentation harder.

Both background subtraction and averaging improve the image quality significantly but even in the finished image there is still a sizeable amount of noise present. Two types stand out: regions where the phase distance is negative or positive and circular waves. It seems like the first is a change in the surface plane, which was not captured. Increasing the polynomial fit could improve this but would lead to overfitting to the bacteria. The second are disturbances at different focal distances, they could in principle be subtracted by isolating them at their focus point and then propagating them to the bacteria's focus point. However, since we were not able to recreate the propagation algorithm which is used by Koala this was not feasible.

5.2 Segmentation and lineage tracking

Properly segmenting phase images gets progressively harder the fuller the image is. As soon as there are clusters of bacteria, boundaries are not clear anymore. The human eye can segment very well by inferring from a wide variety of clues and features. Ilastik is only able to use a small set of predetermined features. As this hinders generalization, the algorithm has been retrained for each experiment, data was only used when dense clusters did not form yet and each used image was visually looked at. Nonetheless, there are still many small mistakes in the segmentation data set. The DeLTA U-Net also learned these mistakes as these segmented images acted as training images. This approach allowed the segmentation of many images (~ 1300) in a reasonable time frame. In retrospect, it would be more reasonable to train fewer images but have more focus on each image and also use a higher variety of experiments and strains of bacteria. The quantity of images can be artificially increased with data augmentation.

When looking at the segmentation results it becomes apparent that sometimes a split is recognised and in the next image the bacteria is rejoined again into one. This was also recognised in the DeLTA paper as a problem (O'Connor et al., 2022). A potential solution could be waiting a longer time between the images, such that the growth of the bacteria is more obvious. Another solution would be adding a temporal component to the segmentation mask, such as the previous image or previous segmentation.

6 Conclusion and outlook

The primary objective of establishing a pipeline, which starts with holograms and stops with the segmentation and tracking of bacteria, has been successfully achieved. Noteworthy enhancements have been introduced when compared to previous workflows. Specifically, the inclusion of a focus-detection technique has significantly improved the accurate determination of focus distance. Furthermore, it has been demonstrated that automating segmentation and tracking of phase images is possible with a U-Net. However, it should be noted that the U-Net's performance has not shown significant improvement, most likely due to its reliance on semi-automatically generated training data, resembling the methodology employed in prior work. It is plausible that superior segmentation results could be obtained by manually creating the training data. Variance in this smaller but correct dataset is then added with data augmentation.

Presently, DeLTA is trained on a single bacterial strain for training and another for validation. Expanding the training dataset to encompass various bacterial strains would probably be worth the effort.

Another possible extension involves the incorporation of different image types, such as bright-field or fluorescent images, for the segmentation task. They could offer more distinct boundaries, potentially leading to a smoother segmentation process.

Furthermore, it is worth considering the possibility of extending our analysis into three-dimensional space. Currently, all bacteria are situated on the surface of the sample, resulting in a single reconstruction plane. Expanding our capabilities to track and calculate the mass of bacteria in three dimensions could offer valuable insights into their behavior and interactions.

References

- Sattar Taheri-Araghi, Suckjoon Jun, Petra Anne Levin, Serena Bradde, Norbert S. Hill, Massimo Vergassola, Johan Paulsson, and John T. Sauls. Cell-Size Control and Homeostasis in Bacteria. *Current Biology*, 27(9):1392, 2017. ISSN 09609822. 10.1016/j.cub.2014.12.009.Cell-size.
- Hai Zheng, Yang Bai, Meiling Jiang, Taku A. Tokuyasu, Xiongliang Huang, Fajun Zhong, Yuqian Wu, Xiongfei Fu, Nancy Kleckner, Terence Hwa, and Chenli Liu. General quantitative relations linking cell growth and the cell cycle in *Escherichia coli*. *Nature Microbiology*, 5(8):995–1001, 2020. ISSN 20585276. 10.1038/s41564-020-0717-x. URL <http://dx.doi.org/10.1038/s41564-020-0717-x>.
- Enno R. Oldewurtel, Yuki Kitahara, and Sven van Teeffelen. Robust surface-to-mass coupling and turgor-dependent cell width determine bacterial dry-mass density. *Proceedings of the National Academy of Sciences of the United States of America*, 118(32), 2021a. ISSN 10916490. 10.1073/pnas.2021416118.
- Yong Keun Park, Christian Depeursinge, and Gabriel Popescu. Quantitative phase imaging in biomedicine. *Nature Photonics*, 12(10):578–589, 2018. ISSN 17494893. 10.1038/s41566-018-0253-x. URL <http://dx.doi.org/10.1038/s41566-018-0253-x>.
- Christina Karlsson Rosenthal, Arianne Heinrichs, Natalie de Souza, Noah Gray, Nicole Rusk, Kim Baumann, Christiaan van Ooij, Alison Schuldt, Emily J. Chenette, Allison Doerr, Silvia Grisendi, Stefano Tonzani, Katherine Whalley, Nathalie Le Bot, Rachel David, Daniel Evanko, Katharine H. Wrighton, Francesca Cesari, and Natalie de Souza. nature Milestones — Light microscopy, 10 2009. URL http://light.ece.illinois.edu/ECE564/_OK_Lectures/00_Timeline_milestones.pdf.
- Dennis Gábor. A New Microscopic Principle. *Nature*, 161(4098):777–778, 1948.
- Emmett N. Leith and Juris Upatnieks. Reconstructed Wavefronts and Communication Theory*. *Journal of the Optical Society of America*, 52(10):1123, 1962. ISSN 0030-3941. 10.1364/josa.52.001123.
- Teresa Cacace, Vittorio Bianco, and Pietro Ferraro. Quantitative phase imaging trends in biomedical applications, 12 2020. ISSN 01438166.
- Su A. Yang, Jonghee Yoon, Kyoohyun Kim, and Yong Keun Park. Measurements of morphological and biophysical alterations in individual neuron cells associated with early neurotoxic effects in Parkinson’s disease. *Cytometry Part A*, 91(5):510–518, 2017. ISSN 15524930. 10.1002/cyto.a.23110.
- Youngchan Kim, Hyoeun Shim, Kyoohyun Kim, Hyun Joo Park, Seongsoo Jang, and Yong Keun Park. Profiling individual human red blood cells using common-path diffraction optical tomography. *Scientific Reports*, 4, 2014. ISSN 20452322. 10.1038/srep06659.

- Arkadiusz Kuś, Michał Dudek, Björn Kemper, Małgorzata Kujawińska, and Angelika Vollmer. Tomographic phase microscopy of living three-dimensional cell cultures. *Journal of Biomedical Optics*, 19(04):1, 2014. ISSN 15602281. 10.1117/1.jbo.19.4.046009.
- J. R. Fienup. Phase retrieval algorithms: a comparison. *Applied Optics*, 21(15):2758, 1982. ISSN 0003-6935. 10.1364/ao.21.002758.
- Zhuo Wang, Larry Millet, Mustafa Mir, Huafeng Ding, Sakulsuk Unarunotai, John Rogers, Martha U Gillette, and Gabriel Popescu. Spatial light interference microscopy (SLIM). *Opt. Express* 19, 1016–1026 (2011), 19(2):1016–1026, 2011.
- Etienne Cuche, Frédéric Bevilacqua, and Christian Depeursinge. Digital holography for quantitative phase-contrast imaging. *Optics Letters*, 24(5):291–293, 1999a.
- Pierre Marquet, Benjamin Rappaz, Pierre J Magistretti, Etienne Cuche, Yves Emery, Tristan Colomb, and Christian Depeursinge. Digital holographic microscopy: a noninvasive contrast imaging technique allowing quantitative visualization of living cells with subwavelength axial accuracy. *Optics Letters*, 30(5):468–470, 2005.
- Etienne Cuche, Pierre Marquet, and Christian Depeursinge. Simultaneous amplitude-contrast and quantitative phase-contrast microscopy by numerical reconstruction of Fresnel off-axis holograms. *Applied Optics*, 38(34):6994–7001, 1999b.
- Frank Dubois, Cédric Schockaert, Natcaha Callens, and Catherine Yourassowsky. Focus plane detection criteria in digital holography microscopy by amplitude analysis. *Optics Express*, 14(13):5895, 2006. ISSN 10944087. 10.1364/oe.14.005895.
- R. Barer. Interference Microscopy and Mass Determination. *Nature*, 169:366–367, 1952.
- Enno R. Oldewurtel, Yuki Kitahara, and Sven van Teeffelen. Supporting Information Robust surface-to-mass coupling and turgor-dependent cell width determine bacterial dry-mass density Table of Contents SI Methods. *Proceedings of the National Academy of Sciences of the United States of America*, 118(32):41, 2021b.
- Somenath Bakshi, Emanuele Leoncini, Charles Baker, Silvia J. Cañas-Duarte, Burak Okumus, and Johan Paulsson. Tracking bacterial lineages in complex and dynamic environments with applications for growth control and persistence. *Nature Microbiology*, 6(6):783–791, 6 2021. ISSN 20585276. 10.1038/s41564-021-00900-4.
- Stuart Berg, Dominik Kutra, Thorben Kroeger, Christoph N. Straehle, Bernhard X. Kausler, Carsten Haubold, Martin Schiegg, Janez Ales, Thorsten Beier, Markus Rudy, Kemal Eren, Jaime I. Cervantes, Buote Xu, Fynn Beuttenmueller, Adrian Wolny, Chong Zhang, Ullrich Koethe, Fred A. Hamprecht, and Anna Kreshuk. ilastik: interactive machine learning for (bio)image analysis. *Nature Methods*, 16(12):1226–1232, 12 2019. ISSN 15487105. 10.1038/s41592-019-0582-9.

Luc Gabel. Multispectral microscopy image segmentation with U-Net for characterization of L-Form bacteria. Technical report, École polytechnique fédérale de Lausanne, Lausanne, 5 2021.

Jean Baptiste Lugagne, Haonan Lin, and Mary J. Dunlop. Delta: Automated cell segmentation, tracking, and lineage reconstruction using deep learning. *PLoS Computational Biology*, 16 (4):1–18, 2020. ISSN 15537358. 10.1371/journal.pcbi.1007673. URL <http://dx.doi.org/10.1371/journal.pcbi.1007673>.

Owen M. O'Connor, Razan N. Alnahhas, Jean Baptiste Lugagne, and Mary J. Dunlop. DeLTA 2.0: A deep learning pipeline for quantifying single-cell spatial and temporal dynamics. *PLoS Computational Biology*, 18(1):1–18, 2022. ISSN 15537358. 10.1371/journal.pcbi.1009797. URL <http://dx.doi.org/10.1371/journal.pcbi.1009797>.

Da Yang, Anna D. Jennings, Evalynn Borrego, Scott T. Retterer, and Jaan Männik. Analysis of factors limiting bacterial growth in PDMS mother machine devices. *Frontiers in Microbiology*, 9(MAY), 5 2018. ISSN 1664302X. 10.3389/fmicb.2018.00871.

Olaf Ronneberger, Philipp Fischer, and Thomas Brox. U-Net: Convolutional Networks for Biomedical Image Segmentation, 5 2015. URL <http://arxiv.org/abs/1505.04597>.

Evan Shelhamer, Jonathan Long, and Trevor Darrell. Fully Convolutional Networks for Semantic Segmentation. *IEEE Transactions on Pattern Analysis and Machine Intelligence*, 39 (4):640–651, 2017. ISSN 01628828. 10.1109/TPAMI.2016.2572683.

Alexey Dosovitskiy, Philipp Fischer, Jost Tobias Springenberg, Martin Riedmiller, and Thomas Brox. Discriminative unsupervised feature learning with exemplar convolutional neural networks. *IEEE Transactions on Pattern Analysis and Machine Intelligence*, 38(9):1734–1747, 2016. ISSN 01628828. 10.1109/TPAMI.2015.2496141.

Eigenständigkeitserklärung

Die unterzeichnete Eigenständigkeitserklärung ist Bestandteil jeder während des Studiums verfassten Semester-, Bachelor- und Master-Arbeit oder anderen Abschlussarbeit (auch der jeweils elektronischen Version).

Die Dozentinnen und Dozenten können auch für andere bei ihnen verfasste schriftliche Arbeiten eine Eigenständigkeitserklärung verlangen.

Ich bestätige, die vorliegende Arbeit selbständig und in eigenen Worten verfasst zu haben. Davon ausgenommen sind sprachliche und inhaltliche Korrekturvorschläge durch die Betreuer und Betreuerinnen der Arbeit.

Titel der Arbeit (in Druckschrift):

Imaging pipeline for DHM

Verfasst von (in Druckschrift):

Bei Gruppenarbeiten sind die Namen aller Verfasserinnen und Verfasser erforderlich.

Name(n):

Braun

Vorname(n):

Fabian Emmanuel Beda

Ich bestätige mit meiner Unterschrift:

- Ich habe keine im Merkblatt „Zitier-Knigge“ beschriebene Form des Plagiats begangen.
- Ich habe alle Methoden, Daten und Arbeitsabläufe wahrheitsgetreu dokumentiert.
- Ich habe keine Daten manipuliert.
- Ich habe alle Personen erwähnt, welche die Arbeit wesentlich unterstützt haben.

Ich nehme zur Kenntnis, dass die Arbeit mit elektronischen Hilfsmitteln auf Plagiate überprüft werden kann.

Ort, Datum

Zürich, 11.09.2023

Unterschrift(en)



Bei Gruppenarbeiten sind die Namen aller Verfasserinnen und Verfasser erforderlich. Durch die Unterschriften bürgen sie gemeinsam für den gesamten Inhalt dieser schriftlichen Arbeit.